Reactivity assessment of lithium with the different components of novel Si/Ni₃.₄Sn₄/Al/C composite anode for Li-ion batteries

Z. Edfouf [a], M.T. Sougrati [b], C. Fariaut-Georges [a], F. Cuevas [a,*], J.-C. Jumas [b],
T. Hézèque [c], C. Jordy [c], G. Caillon [c], M. Latroche [a]

[a] CMTR-ICMPE, UMR7182, CNRS-UPEC, 2-8 rue Henri Dunant, Thiais 94320, France
[b] ICGM, UMR 5253, CNRS, Université Montpellier II, CC 1700 Place Eugène Bataillon, 34095 Montpellier Cedex 5 France
[c] SAFT Batteries, 113 Bd. Alfred Daney, 33074 Bordeaux, France

HIGHLIGHTS

- Understanding Li reactivity toward $Ni_{0.14}Sn_{0.17}Si_{0.32}Al_{0.037}C_{0.346}$ nano-composite.
- Use powerful *operando* methods to study transformations along Li composite cycling.
- Si forms amorphous Li–Si alloys while $Ni_{3.4}Sn_4$ decomposes reversibly in Li–Sn ones.

GRAPHICAL ABSTRACT
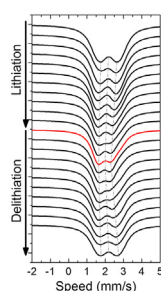
ABSTRACT

Understanding the reactivity of lithium toward new materials proposed for electrodes in lithium ion batteries is an important step to improve material performances. In this work, the reactivity with Li of a new negative electrode material with atomic composition $Ni_{0.14}Sn_{0.17}Si_{0.32}Al_{0.037}C_{0.346}$ is carried out. Powerful characterization methods (*Operando* XRD, Transmission Mössbauer Spectroscopy TMS and Cyclic Voltammetry CV) have been used to investigate electrochemical and structural transformations along cycling. The excellent behavior of this new composite is achieved thanks to the reversible reactions of all components with lithium, namely Si, $Ni_{3.4}Sn_4$ and C phases. Formation of Li–Sn and Li–Si alloys is identified and discussed.

© 2013 Elsevier B.V. All rights reserved.

1. Introduction

The development of advanced rechargeable lithium ion batteries for efficient energy storage to satisfy on board or stationary applications is nowadays a very challenging effort. Actually, most of the lithium ion battery market uses graphite, with a specific capacity of 372 mA h g^{-1} for LiC_6 [1], as negative electrode. To improve the capacity of the negative electrode, various materials are studied as alternatives to carbonaceous materials using conversion reactions with oxides, sulfides, nitrides, phosphides, fluorides [2–8] or hydrides [9–11].

Beside this conversion reaction, a special interest is also devoted to *p*-elements that form lithiated compounds [12]. For example, Sn and Si can form $Li_{4.4}Sn$ and $Li_{4.4}Si$ compounds to store 994 and

4200 mA h g^{-1}, respectively, leading to much higher capacities than graphite [13]. Unfortunately, when used as elemental materials, Sn and Si show large capacity decrease during the first cycles. Indeed, due to the large volume expansion of the materials, Li insertion and extraction upon cycling leads to electrode pulverization and loss of electrical contact [14,15]. To improve mechanical stability, embedding capacitive elements into a matrix able to accommodate the volume expansion is an interesting answer. This concept can be implemented by using binary intermetallic compounds consisting of two elements, one that reacts with lithium and another one that is inactive. The presence of the metallic phase will also improve the electric conductivity within the electrode. Moreover, if the active material is downsized to nanoscale, this shortens the diffusion length for lithium insertion and increases the surface area of the active material leading to faster Li mobility and lower charge transfer resistance of the electrode [16,17].

Recently, a nanostructured composite with atomic composition $Ni_{0.14}Sn_{0.17}Si_{0.32}Al_{0.037}C_{0.346}$ has been prepared as anode material for Li-ion battery [18,19]. Aluminum was added in low quantity (3.7 at.%) to improve cycle-life [20]. The composite is obtained by ball milling pure silicon, intermetallic tin-containing compound $Ni_{3.4}Sn_4$, aluminum and carbon. The nanostructured composite consists of Si particles of about 150 nm in size embedded in a poorly crystallized and complex multi-elemental matrix mostly composed by the intermetallic phase $Ni_{3.4}Sn_4$, Al and disordered carbon. This composite shows a high reversible capacity (920 mA h g^{-1}) with reasonable capacity retention over 280 cycles (0.14% loss per cycle) and very good kinetics. Moreover, the average potential is well-adapted for a negative electrode: 0.4 V vs. Li$^+$/Li^0. Fig. 1 (from Ref. [19]) shows the evolution of the potential versus gravimetric capacity for the first lithiation (C/50) of the active material. This capacity refers to the ball-milled composite and after subtraction of the carbon black contribution used in the electrode formulation. The capacity reaches 1586 mA h g^{-1} for this first cycle and the lithiation profile shows two stages. The first one between 2 and 0.5 V shows a steep drop corresponding to the material activation and the second one between 0.5 and 0 V exhibits a slightly decreasing plateau. This plateau can be attributed to the lithiation of two phases: Si and $Ni_{3.4}Sn_4$. Indeed, nanosized Si forms Li$_x$Si alloys at low potential, mainly $Li_{12}Si_7$ at 0.1 V. Moreover, the lithiation of the $Ni_{3.4}Sn_4$ metallic phase has been already investigated [21–28] and also shows a lithiation plateau below 0.5 V. Upon cell charging (i.e. delithiation reaction), a capacity of 1259 mA h g^{-1} is restored. The irreversible capacity for the first cycle is around 20.6% corresponding to the SEI layer formation.
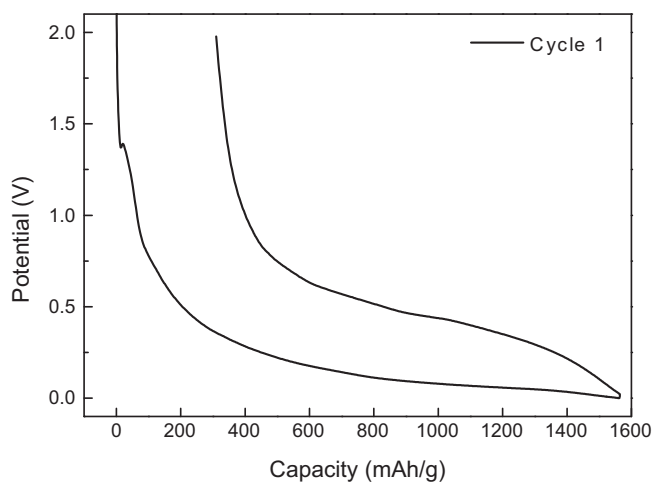
In this composite, all phases (Si, $Ni_{3.4}Sn_4$, and carbon) may react reversibly with lithium and contribute in a cooperative way to the total electrochemical capacity. For a better understanding of the underlying reaction mechanisms, detailed electrochemical and structural analysis are needed. Using powerful characterization methods (Cyclic Voltammetry CV, operando X-Ray Diffraction XRD and operando ^{119}Sn Transmission Mössbauer Spectroscopy TMS), we investigated the material reactivity with lithium and we propose from the results a mechanism for the reversible formation of the lithiated phases.

2. Experimental

2.1. Preparation of the electrode material

The nanostructured composite $Ni_{0.14}Sn_{0.17}Si_{0.32}Al_{0.037}C_{0.346}$ was prepared by a two-step procedure. First, a tin based intermetallic precursor $Ni_{3.4}Sn_4$ was synthesized by powder metallurgy followed by mechanical milling in a Fritsch P7 planetary mill of the precursor with silicon (purity 99.9%; <1 μm), aluminum (purity 99%, ≤75 μm, Aldrich) and graphite in the weight ratio 66.8%, 21.1%, 2.3% and 9.8%, respectively. Ball milling was performed under argon atmosphere for 20 h (with resting periods of 20 min every hour) in a
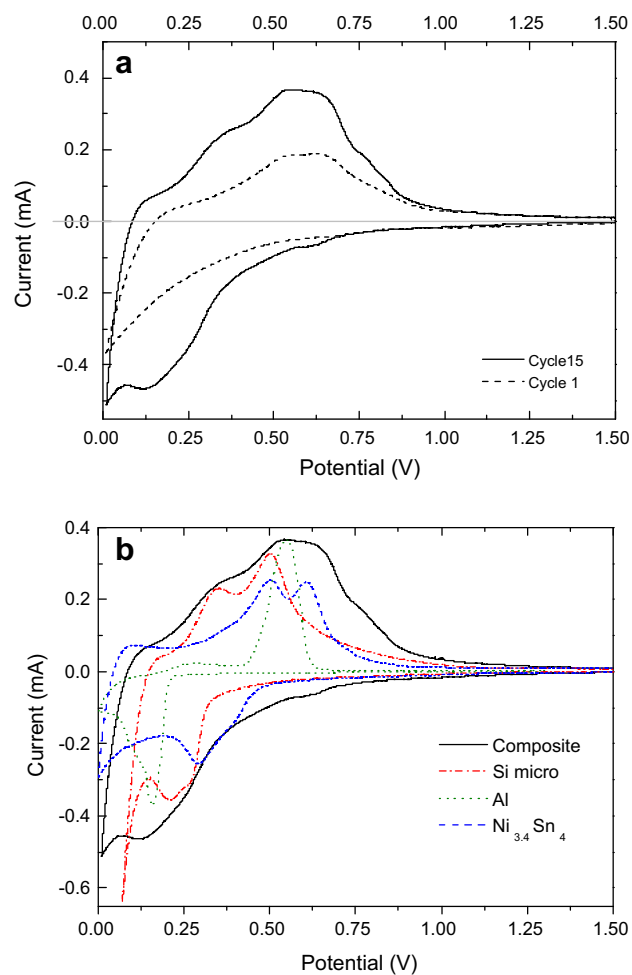

Fig. 1. Galvanostatic charge–discharge lithiation profile (first cycle at C/50) for the nanostructured composite $Ni_{3.4}Sn_4$ + Si + Al + C with nominal atomic composition $Ni_{0.14}Sn_{0.17}Si_{0.32}Al_{0.037}C_{0.346}$ (Data from Ref. [19]).

Fig. 2. Cyclic voltammetry at 0.1 mV s^{-1} for the nanostructured composite $Ni_{3.4}Sn_4$ + Si + Al + C (a) at the first and fifteenth cycle (b) at the fifteenth cycle compared to the various constituents of the composite in micrometric size.

35 ml volume jar made of hardened steel with 7 mm diameter stainless steel balls. The ball to powder weight ratio is 5:1. Vial rotation speed of the mill is 600 rpm. Further details on the preparation and characterization of the composite can be found in Ref. [19].

2.2. Electrodes used for CV measurements

The active material was prepared by mixing 40 wt% of the ball-milled composite sieved under 36 μm, 30 wt% of a fine powder of carboxymethyl-cellulose (CMC) as binder, and 30 wt% of carbon black. Low composite loading in the electrode formulation (40 wt%) was expressly chosen to ascertain the intrinsic reaction mechanisms toward lithiation by minimizing electrical conductivity and mechanical stability concerns. The cell was made of i) a working electrode prepared from a piece of copper foil (18 mm in diameter), coated beforehand with an ink made of the active material, calendered to 2 mg cm^{-2} and air dried in ambient temperature during approximately 3 h, ii) a separator made of a Whatman GF/A borosilicate glass fiber sheet saturated with 50 μl of electrolyte (LiPF$_6$ 1 M) dissolved in an organic solution of ethyl-carbonate (EC), propylene-carbonate (PC) and dimethyl-carbonate (DMC) in volume proportions (1/1/3) and iii) a Li metal disk as negative electrode. This stacking was positioned into a Swagelok®-type cell composed of two parts: a plastic body (couplings and joints) and two metallic current collectors. The crimping of the cell was done under argon atmosphere in a glove box.

Cyclic Voltammetry was made at a scan rate of 0.1 mV s^{-1} in a potential window between 0 and 1.5 V. For reference purposes, micrometric powders of Si, Al and Ni$_{3.4}$Sn$_4$ were analyzed under the same electrochemical conditions.

2.3. Operando experiments

The electrode material was prepared by mixing manually in an agate mortar 55 wt% of the composite, 20 wt% a fine powder of carboxymethyl-cellulose (CMC) as binder and 25 wt% of carbon black. The separator was the same than that used for the CV experiments (Whatman GF/A soaked in electrolyte). *Operando* XRD and Mössbauer experiments require an electrochemical mounting adapted for the passage of X- and γ-rays through the cell to interact with the active material during the analysis. For this purpose, a specially designed cell developed by J.B. Leriche at LRCS in Amiens (France) [29] was used. This cell is equipped with a beryllium window located directly on top of the active material.

Sn-containing phases were investigated by room temperature Transmission ^{119}Sn Mössbauer Spectroscopy (TMS). TMS measurements were carried out at room temperature in the constant acceleration mode with an EG&G spectrometer using a Ca^{119m}SnO$_3$ γ-ray source with a nominal activity of 370 MBq. The isomer shifts are given relative to BaSnO$_3$ standard. A spectrum was recorded every 40 min, but a better statistic is obtained when spectra are integrated for a period of 3 h 20 min. All spectra were refined with Lorentzian profiles, by the least-squares method using the Fullham software (R.P. Hermann), and the quality of the fit was controlled by the usual χ^2 test. The maximum experimental error on hyperfine parameters is estimated to ±0.05 mm s^{-1}.

Operando XRD analysis was made at room temperature with a X'Pert MPD θ-2θ diffractometer (PANalytical) equipped with a X'celerator detector, a copper K$_\alpha$ anode and a Nickel K$_\beta$ filter. Galvanostatic cycling was performed with a VMP3 potentiostat from Biologic®, Claix (France) between 2 and 0 V. A diffractogram was recorded every 2 h.
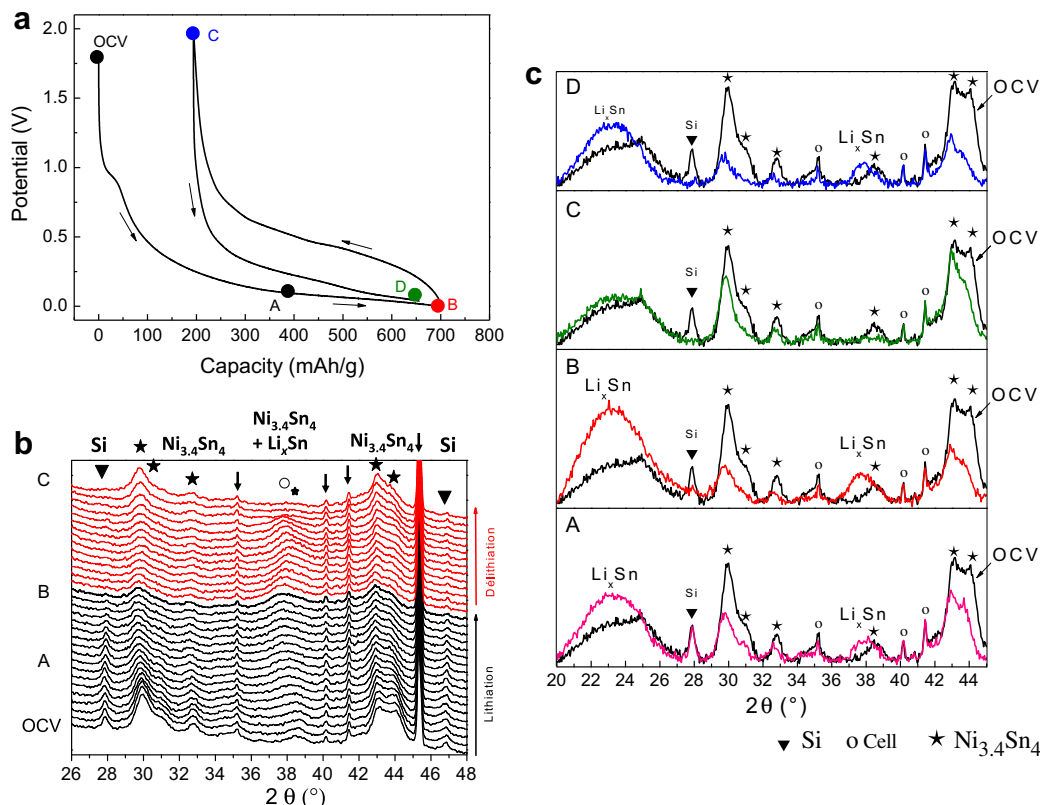

Fig. 3. (a) Galvanostatic charge–discharge lithiation profile (C/50) for the first discharge/charge and second discharge cycles of the composite Ni$_{3.4}$Sn$_4$ + Si + Al + C during *operando* XRD experiment; (b) Evolution of the XRD patterns of the composite at different steps of the lithiation/delithiation and showing the different involved phases; (c) Comparison of the XRD patterns of the composite at different state of lithiation and delithiation (labeled A, B, C and D in Fig. 3a) with the XRD pattern obtained before cycling at open circuit voltage (OCV) with ▼: Si; ○: *operando* cell; ★: Ni$_{3.4}$Sn$_4$.

3. Results

The electrochemical properties of the nanostructured composite $Ni_{0.14}Sn_{0.17}Si_{0.32}Al_{0.037}C_{0.346}$ was first studied by CV to understand the reaction mechanisms that occur during electrochemical cycling. Fig. 2a shows the first and the fifteenth cyclic voltammograms of the composite. The first cyclic voltammetric curve (dotted line)

shows rather low currents and does not exhibit characteristic lithiation peak indicating that the material does not react completely. During this very first cycle, the material activates and the SEI layer is formed. The reversible lithiation reactions are better observed during the fifteenth cycle (Fig. 2a, full line). The profile shows several current peaks that are attributed to the redox reactions of different active phases contained in the composite and
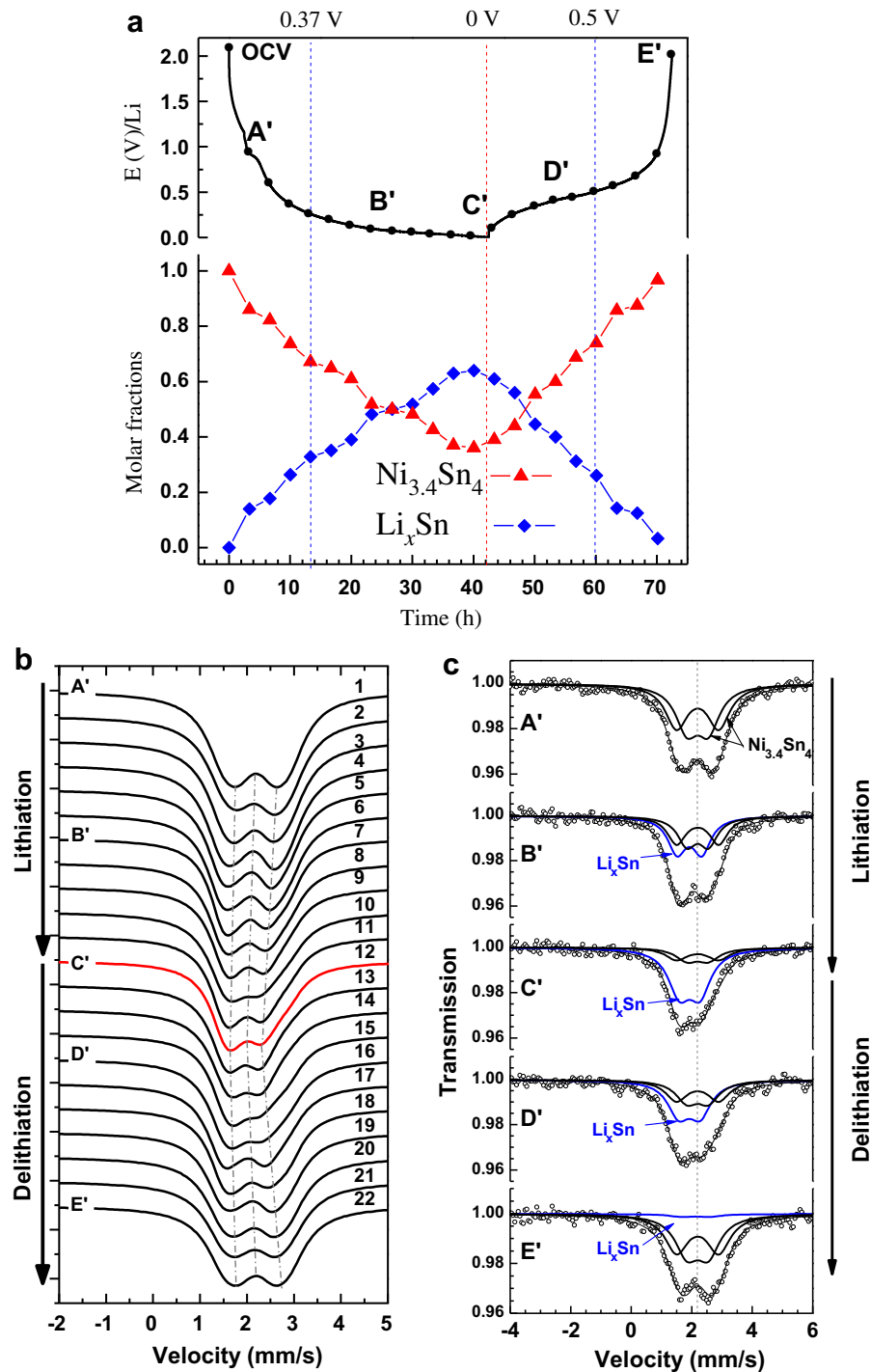

Fig. 4. (a) (top) First galvanostatic cycle made during the ^{119}Sn *operando* Mössbauer analysis with the different points (A′ to E′) corresponding to the data refined in 4c, and (bottom) molar fractions of the $Ni_{3.4}Sn_4$ and Li_xSn phases in the composite $Ni_{3.4}Sn_4$ + Si + Al + C deduced from the *operando* Mössbauer analysis; (b) Evolution of the ^{119}Sn Mössbauer spectra of the composite during the first cycle; (c) Selected ^{119}Sn Mössbauer spectra refined with two contribution ($Ni_{3.4}Sn_4$ and Li_xSn phases) showing the lithiation and delithiation of the $Ni_{3.4}Sn_4$ phase.

contributing to the total capacity of the material. Indeed, Fig. 2b can be reasonably explained by the convolution of different cyclic voltammetric curves obtained for the various constituents of the composite (micrometer-sized Si, $Ni_{3.4}Sn_4$ and Al) leading to a good agreement between the individual phase contributions and the composite curve. From this observation, it is clear that all constituents are active toward lithium (both the Si particles and the multi-elementary matrix around them), which explains the high capacity obtained for this composite.

The two first electrochemical cycles have been investigated by *operando* XRD analysis. Fig. 3a shows the profile of the first discharge/charge (between 2 and 0 V) followed by the second discharge of the composite.

The first diffractogram was registered in open circuit voltage (OCV). Fig. 3b shows the diffractogram evolution as a function of the state of charge. The diffraction peak intensities of Si (at $2\theta \sim 28°$ and $\sim 47°$) gradually decrease and finally vanish at the end of the discharge and do not show up again. Similarly, diffracted intensities of the $Ni_{3.4}Sn_4$ phase decrease during lithiation. This phenomenon is clearly visible for the two double peaks located in the range 29–32° and 42–45° in 2θ. Finally, another peak located at 38.5° shifts to smaller angles and gains in intensity during lithiation. This is attributed to the formation of intermetallic alloys of Li_xSn-type whose main diffraction peak are close to that of $Ni_{3.4}Sn_4$ at $\sim 38.5°$, such convolution leading to the shift effect. Upon delithiation, these changes are reversible since the peaks assigned to Li_xSn alloys disappear while the peaks of the $Ni_{3.4}Sn_4$ phase regain in intensity. However, Si diffraction peaks do not recover indicating that silicon gradually becomes amorphous.

For a better understanding, the most interesting diffractograms obtained during lithiation and delithiation (labeled A, B, C and D in Fig. 3a) are detailed and compared in Fig. 3c. The diffractogram obtained after lithiation at 0.1 V (A) and compared with the first one (OCV before cycling) confirms the decrease of the diffraction peak intensities of the $Ni_{3.4}Sn_4$ phase and the appearance of the Li_xSn alloys. Position and intensity of the Si peaks do not change which means that silicon does not react with lithium down to 0.1 V. At 0 V (B), the peaks corresponding to the Li_xSn alloys (20–26° and 37–39°) raise. These peaks can be assigned to the formation of lithium-rich alloys from Li_5Sn_2 ($x = 2.5$) to Li_7Sn_2 ($x = 3.5$) at the end of the lithiation. We also note that the Si peaks vanish indicating that this element starts reacting with lithium below 0.1 V. After delithiation up to 2 V (C), the Li_xSn alloy peaks disappear whereas the $Ni_{3.4}Sn_4$ ones reappear though they are weaker in intensity as compared to the pristine composite. Diffractogram in C is therefore rather comparable to A except for silicon that remains not observable. Finally, the last diffractogram (D) is obtained at the end of the second lithiation. It is very comparable to diffractogram B showing that the reaction involving the nickel–tin phase is fully reversible on charging/discharging.

The electrode material behavior was then further analyzed by *operando* Transmission Mössbauer Spectroscopy. The cycling profile is presented in Fig. 4a with data labels (A′ to E′) referring to the Mössbauer spectra in Fig. 4b and c. Evolution of the Mössbauer spectra during the electrochemical (de)lithiation can be followed in Fig. 4b. One can observe the global transformations occurring during the electrochemical cycle. Three dotted lines have been added as guides to the eye showing the progressive decrease (increase) of the isomer shift during lithiation (delithiation). The most significant spectra (A′ to E′) have been refined assuming two tin phases $Ni_{3.4}Sn_4$ and Li_xSn and are detailed in Fig. 4c.

First, one can see the reactivity of the $Ni_{3.4}Sn_4$ phase from A′ to C′ (end of lithiation). The intensity of the two characteristic doublets of $Ni_{3.4}Sn_4$ decreases while the Li_xSn phase contribution appears. This reaction is not completed in C′ since a small quantity of $Ni_{3.4}Sn_4$

phase is still detected at the end of the lithiation. During delithiation (from D′ to E′), the contributions are inverted, demonstrating the reversibility of the reaction. In Fig. 5, the hyperfine parameters deduced from the fitted spectra as well as the spectral absorption are compared at different steps of the electrochemical cycle and the detailed results are given in Table 1. Evolution of the hyperfine parameters can be separated in four different regions noted R1 to R4 in Fig. 5.

In the first region R1, a decrease of the isomer shift of the Li_xSn phase is noted signing the appearance of a Li-rich alloy due to the lithiation of the $Ni_{3.4}Sn_4$ phase. In the second range R2, both quadrupole splitting of the Li_xSn phase and absorption by the electrode decrease significantly while the isomer shift remains stable. This observation indicates the progressive enrichment of the Li_xSn phase in lithium. In areas R3 and R4, a reversed evolution of the hyperfine parameters is observed (though absorption increases slightly) in agreement with the reversibility of the reaction. From the refined data, a quantification of the tin phases present in the material was carried out and the results are shown in Fig. 4a and Table 1. It is clearly shown that, on discharge, the amount of $Ni_{3.4}Sn_4$ decreases and that of Li_xSn increases, whereas, on charge, the opposite trend is observed. This confirms the same reactivity for the $Ni_{3.4}Sn_4$ and Li_xSn phases as observed by *operando* XRD analysis. However, this is only an approximation since we used a unique and
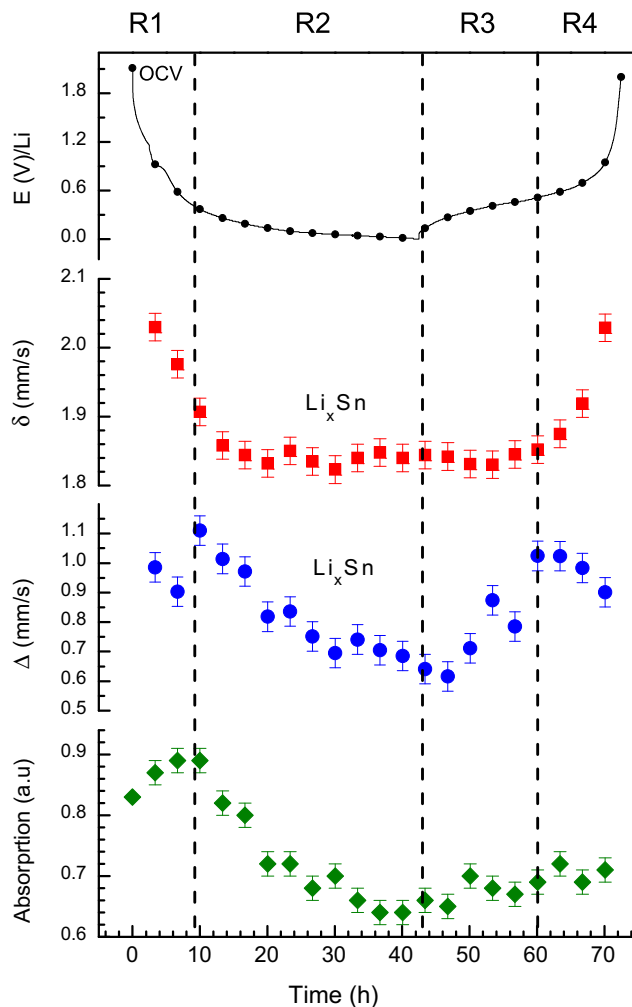

Fig. 5. Hyperfine parameters of the Mössbauer spectra and spectral absorption of the composite $Ni_{3.4}Sn_4$ + Si + Al + C.

Table 1
Hyperfine parameters of the Mössbauer spectra shown in Fig. 4b for the composite $Ni_{3.4}Sn_4 + Si + Al + C$: δ (isomer shift relative to $BaSnO_3$), Δ (quadrupole splitting), relative areas (R. A.) and the corresponding molar fractions (Mol. frac.) after corrections using the Lamb–Mössbauer factors. The selected spectra A′ to E′ shown in Fig. 4c correspond to spectra 1, 7, 13, 16 and 22, respectively.

Spectrum	Phases	δ (mm s^{-1})	Δ (mm s^{-1})	R. A. (%)	Mol. frac. (mol%)	Spectrum	δ (mm s^{-1})	Δ (mm s^{-1})	R. A. (%)	Mol. frac. (mol%)
1A′	Li_xSn	–	–	0	0	12	1.84	0.69	63	76
	$Ni_{3.4}Sn_4$	2.22	0.77	50	100		2.22	0.77	18.5	24
		2.22	1.42	50			2.22	1.42	18.5	
2	Li_xSn	2.03	0.98	14	23	**13C′**	1.84	0.64	64	76
	$Ni_{3.4}Sn_4$	2.22	0.77	43	77		2.22	0.77	18	24
		2.22	1.42	43			2.22	1.42	18	
3	Li_xSn	1.90	1.11	18	28	14	1.84	0.62	61	74
	$Ni_{3.4}Sn_4$	2.22	0.77	41	72		2.22	0.77	19.5	26
		2.22	1.42	41			2.22	1.42	19.5	
4	Li_xSn	1.86	1.01	26	39	15	1.83	0.71	56	70
	$Ni_{3.4}Sn_4$	2.22	0.77	37	61		2.22	0.77	22	30
		2.22	1.42	37			2.22	1.42	22	
5	Li_xSn	1.84	0.97	33	47	**16D′**	1.83	0.87	45	59
	$Ni_{3.4}Sn_4$	2.22	0.77	33.5	53		2.22	0.77	27.5	41
		2.22	1.42	33.5			2.22	1.42	27.5	
6	Li_xSn	1.83	0.82	35	50	17	1.85	0.78	40	55
	$Ni_{3.4}Sn_4$	2.22	0.77	32.5	50		2.22	0.77	30	45
		2.22	1.42	32.5			2.22	1.42	30	
7B′	Li_xSn	1.85	0.84	39	54	18	1.85	1.02	31	45
	$Ni_{3.4}Sn_4$	2.22	0.77	30.5	46		2.22	0.77	34.5	55
		2.22	1.42	30.5			2.22	1.42	34.5	
8	Li_xSn	1.84	0.75	48	63	19	1.87	1.02	26	39
	$Ni_{3.4}Sn_4$	2.22	0.77	26	37		2.22	0.77	37	61
		2.22	1.42	26			2.22	1.42	37	
9	Li_xSn	1.82	0.69	50	65	20	1.92	0.98	14	23
	$Ni_{3.4}Sn_4$	2.22	0.77	25	35		2.22	0.77	43	77
		2.22	1.42	25			2.22	1.42	43	
10	Li_xSn	1.84	0.74	52	66	21	2.03	0.90	13	21
	$Ni_{3.4}Sn_4$	2.22	0.77	24	34		2.22	0.77	43.5	79
		2.22	1.42	24			2.22	1.42	43.5	
11	Li_xSn	1.85	0.70	57	71	**22E′**	2.03	0.90	33	6
	$Ni_{3.4}Sn_4$	2.22	0.77	21.5	29		2.22	0.77	33.5	94
		2.22	1.42	21.5			2.22	1.42	33.5	

average Li_xSn phase with refined hyperfine parameters to account for the different Li–Sn alloys formed during cycling.

Despite the fact that the spectra are difficult to adjust by single phases due to the coexistence of several phases with very similar signatures, we refined some spectra with either Li_7Sn_3, Li_5Sn_2 or Li_7Sn_2 phases beside $Ni_{3.4}Sn_4$ during lithiation (from 0.37 to 0 V). Characteristic isomer shifts and quadrupole splitting of the previous Li–Sn compounds was used as input data [30]. The refined spectra are shown in Fig. 6. Results of the refinements are presented in Table 2. This analysis shows the foremost presence of Li_7Sn_3 around 0.2 V, followed by Li_5Sn_2 at 0.09 V and Li_7Sn_2 at the end of the lithiation. The amount of $Ni_{3.4}Sn_4$ which has not reacted at the end of the lithiation is about 7 mol%.

4. Discussion

The composite made from the ball milling of Si, $Ni_{3.4}Sn_4$, aluminum and carbon shows a high reversible capacity (920 mA h g^{-1}) with good capacity retention and low potential (~0.4 V), making this material suitable for negative electrode in Li-ion batteries. From the present study using CV, *operando* XRD and TMS, a better understanding of the reaction paths can be drawn. It is first interesting to look at the total capacity of the composite. According to the composition and to the upper lithiation value of each constituent, a theoretical value can be derived (Table 3) leading to a maximum capacity of 1409 mA h g^{-1}. However, recent investigations [31] have proved that the richest Li–Si alloy formed electrochemically at room temperature is rather $Li_{15}Si_4$ than $Li_{4.4}Si$. Similarly, according to our TMS study, the richest alloy formed with

Sn is more likely Li_7Sn_2 than $Li_{4.4}Sn$. Accordingly, if one substitutes 4.4 Li by 3.75 for Si and by 3.5 for Sn in Table 3, the capacity for the composite drops to 1183 mA h g^{-1}. Such expected value agrees well with the value reported in the present work (1259 mA h g^{-1} for the first delithiation), showing that silicon alone cannot account for the whole capacity and demonstrating that the complex multi-elemental matrix made of the metallic phase $Ni_{3.4}Sn_4$, aluminum and disordered carbon participates also to the electrochemical process. This statement is also confirmed by CV measurements (Fig. 2b).

Moreover, from the *operando* XRD and TMS analysis, it appears clearly that most of the reactions are reversible despite the fact that differences in capacities are observed for *operando* experiments (Fig. 3a) as compared to conventional galvanostatic cycling (Fig. 1) because the use of bulk electrode material leads to less efficiency than the thin inked ones. The intermetallic phase $Ni_{3.4}Sn_4$ decomposes with lithium to form Li–Sn alloys and probably free metallic nickel though X-ray diffraction does not allow characterizing this element after lithiation. It is then probably worth to admit that nickel is in an amorphous state in the matrix but close enough to the Li–Sn alloys to be able to recombine restoring the $Ni_{3.4}Sn_4$ phase upon delithiation. Therefore, the $Ni_{3.4}Sn_4$ phase in the studied composite follows a conversion mechanism which contributes significantly to the electrode capacity. The behavior of Si is somewhat different since its diffraction peak intensities gradually decrease to finally disappear at the end of the lithiation and never show up again. Silicon stays in an amorphous state for the remaining part of the experiment and shows excellent reversibility with lithium on cycling.
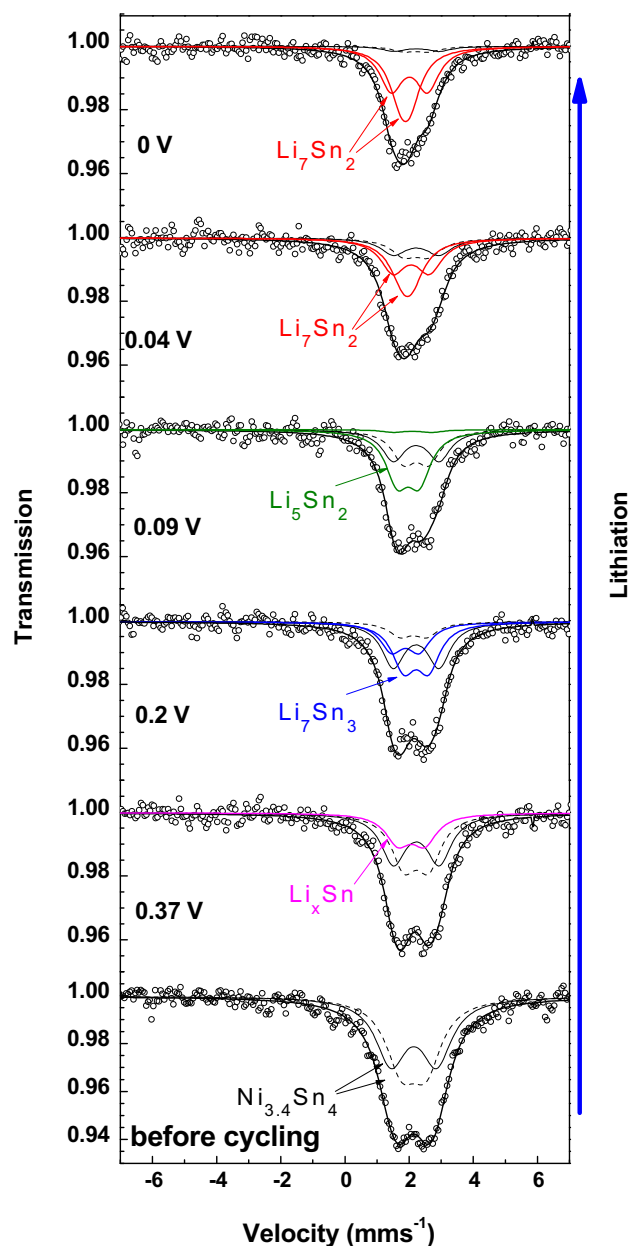
Fig. 6. Selected ^{119}Sn Mössbauer spectra of the composite $Ni_{3.4}Sn_4 + Si + Al + C$ refined with contributions of $Ni_{3.4}Sn_4$, averaged Li_xSn, Li_7Sn_3, Li_5Sn_2 and Li_7Sn_2 phases.

Table 2

Hyperfine parameters of Mössbauer spectra shown in Fig. 6 for the composite $Ni_{3.4}Sn_4 + Si + Al + C$: δ (isomer shift relative to $BaSnO_3$), Δ (quadrupole splitting), relative areas (R. A.) and the corresponding molar fractions (Mol. frac.) after corrections using the Lamb−Mössbauer factors.

Potential (V)	Phases	δ (mm s^{-1})	Δ (mm s^{-1})	R. A. (%)	Mol. frac. (mol%)
OCV	Li_xSn	–	–	0.00	0
	$Ni_{3.4}Sn_4$	2.22	0.77	0.50	100
		2.22	1.42	0.50	
0.37	Li_xSn	2.07	0.83	0.22	30
	$Ni_{3.4}Sn_4$	2.22	0.77	0.39	70
		2.22	1.42	0.39	
0.2	Li_7Sn_3	2.14	0.82	0.11	41
		1.89	0.86	0.21	
	$Ni_{3.4}Sn_4$	2.22	0.77	0.34	59
		2.22	1.42	0.34	
0.09	Li_5Sn_2	1.94	0.70	0.43	56
		2.07	1.20	0.22	
	$Ni_{3.4}Sn_4$	2.22	0.77	0.27	44
		2.22	1.42	0.27	
0	Li_7Sn_2	1.89	0.28	0.45	93
		2.01	1.13	0.45	
	$Ni_{3.4}Sn_4$	2.22	0.77	0.05	7
		2.22	1.42	0.05	

Table 3

Chemical reactions with lithium expected to take place for the different phases in the composite $Ni_{3.4}Sn_4 + Si + Al + C$ and calculated capacities according to the weight ratio of each constituents.

Chemical reactions	C (mA h g^{-1})	Composite (wt.%)	Composite (mA h g^{-1})
$Ni_{3.4}Sn_4 + 17.6Li \rightarrow 4Li_{4.4}Sn + 3.4Ni$	699	67.0	468.4
$Si + 4.4Li \rightarrow Li_{4.4}Si$	4199	21.0	881.7
$Al + Li \rightarrow LiAl$	993	2.3	22.8
$6C + Li \rightarrow LiC_6$	372	9.7	36.1
Total		100.0	1409.0

excellent matrix to embed Si nanoparticles that are more sensitive to degradation by cycling.

5. Conclusion

The composite $Ni_{0.14}Sn_{0.17}Si_{0.32}Al_{0.037}C_{0.346}$ is obtained by ball milling of pure silicon, tin-containing alloy $Ni_{3.4}Sn_4$, aluminum and carbon. It consists of nanometric Si particles embedded in a poorly crystallized and complex multi-elemental matrix made of the phase $Ni_{3.4}Sn_4$, aluminum and disordered carbon. The high capacity is attributed to the lithiation of the main phases Si and $Ni_{3.4}Sn_4$ whereas the good stability is attributed to buffering of electrode volume variations by Ni and C elements. From CV and *operando* XRD and TMS measurements, it is demonstrated that the phase $Ni_{3.4}Sn_4$ reacts with lithium to form Li−Sn alloys up to Li_7Sn_2 and free poorly crystallized nickel. The Li−Sn alloys recombine with Ni to restore the crystalline phase $Ni_{3.4}Sn_4$ following a conversion reaction mechanism. Silicon reacts reversibly with lithium to form amorphous Li−Si alloys without recovering a crystalline state upon delithiation. Lithiation of the major Si and $Ni_{3.4}Sn_4$ phases occur at different potentials, which may facilitate the release of mechanical stress during electrochemical reactions.

Our results show that the major phases of the composite, $Ni_{3.4}Sn_4$ and Si, are active towards lithium at different reaction potentials. Thus, on the first discharge and above 0.1 V, $Ni_{3.4}Sn_4$ starts reacting with lithium to successively form Li_7Sn_3 and Li_5Sn_2 compounds (Fig. 6) before Si undergoes amorphization at lower potentials (Fig. 3c). This fact may help to reach long cycle-life for this composite as result of two phenomena: i) diminution of mechanical stresses due to gradual swelling of the electrode over a wide potential range and ii) enhanced strain release due to a double buffering action between the composite constituents, *i.e.* when the first constituent reacts with lithium at a given potential the second one acts as a buffering matrix and *vice versa*. Still on stability concerns, it is worth mentioning that previous studies show that nanocrystalline $Ni_{3.5}Sn_4$ electrode exhibits outstanding cycle-life over more than 400 cycles [32]. This phase constitutes an

References

[1] Rechargeable lithium batteries (ambient temperature), in: T.B. Reddy, S. Hossain (Eds.), Handbook of Batteries, McGraw-Hill, 2002, pp. 1–62. (Chapter 34).
[2] Q. Sun, Z.-W. Fu, Electrochem. Solid-State Lett. 10 (8) (2007) A189–A193.
[3] Y. Wang, Z.-W. Fuz, X.-L. Yue, Q.-Z. Qin, J. Electrochem. Soc. 151 (4) (2004) E162–E167.
[4] V. Pralong, D.C.S. Souza, K.T. Leung, L.F. Nazar, Electrochem. Commun. 4 (2002) 516–520.
[5] G.G. Amatucci, N. Pereira, J. Fluorine Chem. 128 (4) (2007) 243–262.
[6] P.-L. Taberna, S. Mitra, P. Poizot, P. Simon, J.-M. Tarascon, Nat. Mater. 5 (7) (2006) 567–573.
[7] P. Poizot, S. Laruelle, S. Grugeon, J.-M. Tarascon, J. Electrochem. Soc. 149 (9) (2002) A1212–A1217.
[8] J.-L. Tirado, Mater. Sci. Eng. R 40 (2003) 103–136.
[9] Y. Oumellal, A. Rougier, G.A. Nazri, J.-M. Tarascon, L. Aymard, Nat. Mater. 7 (2008) 916–921.
[10] N. Hanada, A. Kamura, H. Suzuki, K. Takai, T. Ichikawa, Y. Kojima, J. Alloys Compd. 509 (S2) (2011) 584–587.
[11] Y. Oumellal, W. Zaïdi, J.-P. Bonnet, F. Cuevas, M. Latroche, J. Zhang, J.-L. Bobet, A. Rougier, L. Aymard, Int. J. Hydrogen Energy 37 (9) (2012) 7831–7835.
[12] A.N. Dey, J. Electrochem. Soc. 118 (1971) 1547.
[13] L.Y. Beaulieu, K.C. Hewitt, R.L. Turner, A. Bonakdarpour, A.A. Abdo, L. Christensen, K.W. Eberman, L.J. Krause, J.R. Dahn, J. Electrochem. Soc. 150 (2) (2003) A149–A156.
[14] U. Kasavajjula, C. Wang, A.J. Appleby, J. Power Sources 163 (2007) 1003–1039.
[15] J. Wolfenstine, J. Power Sources 79 (1999) 111–113.
[16] A.H. Whitehead, J.M. Elliott, J.R. Owen, J. Power Sources 81–82 (1999) 33–38.
[17] Z. Wang, W.H. Tian, X.H. Liu, Y. Li, X.G. Li, Mater. Chem. Phys. 100 (2006) 92–97.
[18] C. Jordy, G. Caillon, T. Hézèque, C. Audry, F. Cuevas, M. Latroche, Active Material Composition for the Negative Electrode of a Lithium-ion Accumulator, EP2239803 US 2010270497, 2010.
[19] Z. Edfouf, F. Cuevas, M. Latroche, C. Georges, C. Jordy, G. Caillon, T. Hézèque, J.-C. Jumas, M.T. Sougrati, J. Power Sources 196 (2011) 4762–4768.
[20] T.D. Hatchard, J.M. Topple, M.D. Fleischauer, J.R. Dahn, Electrochem. Solid-State Lett. 6 (7) (2003) A129–A132.
[21] X.Q. Cheng, P.F. Shi, J. Alloys Compd. 391 (2005) 241–244.
[22] H.Y. Lee, S.W. Jang, S.M. Lee, S.J. Lee, H.K. Baik, J. Power Sources 112 (2002) 8–12.
[23] S. Naille, C.M. Ionica-Bousquet, F. Robert, F. Morato, P.E. Lippens, J. Olivier-Fourcade, J. Power Sources 174 (2007) 1091–1094.
[24] L. Huang, H.B. Wei, F.S. Ke, X.Y. Fan, J.T. Li, S.G. Sun, Electrochim. Acta 54 (2009) 2693–2698.
[25] H. Mukaibo, T. Mommaa, T. Osaka, J. Power Sources 146 (2005) 457–463.
[26] I. Amadei, S. Panero, B. Scrosati, G. Cocco, L. Schiffini, J. Power Sources 143 (2005) 227–230.
[27] J. Hassoun, S. Panero, B. Scrosati, J. Power Sources 160 (2006) 1336–1341.
[28] S.W. Woo, N. Okada, M. Kotobuki, K. Sasajima, H. Munakata, K. Kajihara, K. Kanamura, Electrochim. Acta 55 (2010) 8030–8035.
[29] J.B. Leriche, et al., J. Electrochem. Soc. 157 (5) (2010) A606–A610.
[30] F. Robert, P.E. Lippens, J. Olivier-Fourcade, J.-C. Jumas, F. Gillot, M. Morcrette, J.-M. Tarascon, J. Solid State Chem. 180 (2007) 339–348.
[31] M.N. Obrovac, L. Christensen, Electrochem. Solid-State Lett. 7 (5) (2004) A93–A94.
[32] Z. Edfouf, C. Fariaut-Georges, F. Cuevas, M. Latroche, T. Hézèque, G. Caillon, C. Jordy, M.T. Sougrati, J.-C. Jumas, Electrochim. Acta 89 (2013) 365–371.